



# Development and validation of a deep learning model for improving detection of nonmelanoma skin cancers treated with Mohs micrographic surgery

Eugene Tan, MBChB,<sup>a,b,c</sup> Sophie Lim, MBBS,<sup>c</sup> Duncan Lamont, MMed,<sup>d</sup> Richard Epstein, MBBS, PhD,<sup>e</sup> David Lim, MBChB,<sup>b</sup> and Frank P. Y. Lin, MBChB, PhD<sup>e,f,g</sup>

**Background:** Real-time review of frozen sections underpins the quality of Mohs surgery. There is an unmet need for low-cost techniques that can improve Mohs surgery by reliably corroborating cancerous regions of interest and surgical margin proximity.

**Objective:** To test that deep learning models can identify nonmelanoma skin cancer regions in Mohs frozen section specimens.

**Methods:** Deep learning models were developed on archival images of focused microscopic views (FMVs) containing regions of annotated, invasive nonmelanoma skin cancer between 2015 and 2018, then validated on prospectively collected images in a temporal cohort (2019-2021).

**Results:** The tile-based classification models were derived using 1423 focused microscopic view images from 154 patients and tested on 374 images from 66 patients. The best models detected basal cell carcinomas with a median average precision of 0.966 and median area under the receiver operating curve of 0.889 at 100x magnification (0.943 and 0.922 at 40x magnification). For invasive squamous cell carcinomas, high median average precision of 0.904 was achieved at 100x magnification.

**Limitations:** Single institution study with limited cases of squamous cell carcinoma and rare non-melanoma skin cancer.

**Conclusion:** Deep learning appears highly accurate for detecting skin cancers in Mohs frozen sections, supporting its potential for enhancing surgical margin control and increasing operational efficiency. (JAAD Int 2024;14:39-47.)

**Key words:** artificial intelligence; basal cell carcinoma; deep learning; digital pathology; Mohs micrographic surgery; squamous cell carcinoma.

From the Western Skin Institute, Melbourne, Australia<sup>a</sup>; Skintel, Auckland, New Zealand<sup>b</sup>; Alfred Health, Melbourne, Australia<sup>c</sup>; Department of Pathology, Waikato Hospital, Hamilton, New Zealand<sup>d</sup>; School of Medicine, University of New South Wales, Sydney, Australia<sup>e</sup>; Kinghorn Centre for Clinical Genomics, Garvan Institute of Medical Research, Sydney, Australia<sup>f</sup>; and NHMRC Clinical Trials Centre, University of Sydney, Camperdown, NSW, Australia.<sup>g</sup>

Funding sources: Dr Lin is supported by an Australian Medical Research Future Fund as part of the Rapid Applied Research Translation initiative (RARUR000125), a Capacity Building Grant funded by Cancer Institute NSW (2021/CBG003), and generous support from the philanthropic funds from the Wolf family (St. Vincent's Curran Foundation).

Prior presentation: Abstracts of this work have previously been presented at the Annual Meetings of the Australian College of Dermatologists in 2022 and 2023, the 2022 annual meeting of

the New Zealand Dermatological Society Inc, the 25th World Congress of Dermatology held in Singapore in 2023, and the New South Wales Cancer Conference in Sydney in 2022.

Patient consent: Not applicable.

IRB approval status: This study for diagnostic model development has approval from the St. Vincent's Hospital Human Research Ethics Committee (2021/ETH00647).

Accepted for publication October 29, 2023.

Correspondence to: Eugene Tan, MBChB, Department of Dermatology, Skintel, 11 Apollo Dr, Rosedale, Auckland, 0632, New Zealand. E-mail: [eugene@skintel.co.nz](mailto:eugene@skintel.co.nz).

2666-3287

© 2023 by the American Academy of Dermatology, Inc. Published by Elsevier Inc. This is an open access article under the CC BY license (<http://creativecommons.org/licenses/by/4.0/>).

<https://doi.org/10.1016/j.jdin.2023.10.007>

## INTRODUCTION

Mohs micrographic surgery (MMS) is the recommended procedure for local high risk basal cell carcinomas (BCCs) and squamous cell carcinomas (SCCs).<sup>1,2</sup> Although excellent concordance exists between MMS surgeons and dermatopathology,<sup>3,4</sup> interobserver discordance may still occur.<sup>5</sup> Variability is seen even amongst experienced surgeons particularly in complex tumors with challenging pathology.<sup>6</sup> As Mohs surgeons often operate in an individual or a small group setting,<sup>7</sup> variable interpretation of frozen sections may also arise due to operator fatigue and/or inconsistent techniques of tissue preparation.

Deep learning has permeated various fields of medicine<sup>8-10</sup> and has demonstrated exceptional performance in the diagnosis of skin diseases on clinical and dermoscopic images.<sup>11-16</sup> It also has the potential to assist Mohs surgeons in optimizing intraoperative margin control through reduction of interobserver discordance<sup>17</sup> but few studies have examined the application of deep learning on Mohs frozen section images.<sup>18</sup>

Here we report on the development of deep learning models that detect nonmelanoma skin cancers (NMSCs) on frozen sections obtained during MMS. These models were trained on a dataset consisting of archival microscope images and routine diagnostic setups and procedures. The primary objective was to validate these models develop models as a first step towards the longer-term objective of enhancing Mohs surgical workflow.

## METHODS

### Study design

This study for diagnostic model development was approved by the St. Vincent's Hospital Human Research Ethics Committee (2021/ETH00647). This research is reported in accord with CLEAR Derm Consensus guidelines for artificial intelligence (AI) algorithm reports in dermatology<sup>19</sup> and Transparent Reporting of a multivariable prediction model for Individual Prognosis Or Diagnosis statement<sup>20</sup> (Supplementary Tables I and II, available via

Mendeley at <https://data.mendeley.com/datasets/fh7sk5ksmk/2>).

### Study population

All patients who had undergone MMS for NMSC in 2015 to 2021 at a Mohs surgical unit in Melbourne, Australia and consented to research during surgery, were identified. The cases were included with diagnostic labels assigned based on the tumor observed during Mohs surgery.

**Cohort and image data.** Archival images of skin lesions from patients who underwent surgery prior to the study's conception (February 20, 2015-December 1, 2018) were used for model development (development cohort). Patients who had been seen after the index date (January 24, 2019-

December 6, 2021) were used for testing model performance (validation cohort). Nonidentifiable demographic data were collected for the cohort characterization.

All pathology slides were prepared using a protocol of progressive Mayer's hematoxylin and eosin stain<sup>21</sup> on EpreDia Linistat Linear Stainer, Fisher Scientific Pittsburgh, PA 15,275. Images of focused microscope view (FMV) were acquired using Leica ICC50 W, 5.0-megapixel Camera attached to DM1000 microscope and captured via the Leica software (LAS-EZ v3.0). Full color images (at 1600 × 1200 pixels resolution) were acquired at 40× and 100× magnification levels. The diagnosis was made by the lead author at the time of surgery. Air bubbles and freezing artifacts were unprocessed during model training to enhance procedural generalizability.

**Image processing and training of deep learning models.** The pipeline was designed to localize regions of malignant lesions on digitized images of FMV by producing an overlaying saliency map indicating the probability of containing tumor. Detection of tumor was performed through a tile-based classification method that utilized the sliding prediction window technique. By incorporating overlapping predictions, the sliding window technique aims to produce more accurate contours for the predicted regions and minimize any potential omissions. All models were based on a convolutional neural network architecture, utilizing the feature extraction layers from EfficientNet B0<sup>22</sup>

## CAPSULE SUMMARY

- Mohs surgery is an effective procedure for nonmelanoma skin cancers but remains labor-intensive, time consuming, and costly.
- Deep learning facilitated margin-control appears to be a valuable addition to Mohs surgery, given its potential for improving resectional efficacy and reliability while minimizing extent, duration, and cost.

*Abbreviations used:*

|        |  |
|--------|--|
| AI:    | artificial intelligence                                |
| AUPRC: | area under the precision-recall curve                  |
| AUROC: | area under the receiver-operating characteristic curve |
| BCC:   | basal cell carcinoma                                   |
| FMV:   | focused microscopic view                               |
| LOOCV: | leave-one-out cross-validation                         |
| MMS:   | Mohs micrographic surgery                              |
| NMSC:  | nonmelanoma skin cancer                                |
| SCC:   | squamous cell carcinoma                                |
| WSL:   | weakly supervised learning                             |

or MobileNetV2<sup>23</sup> models concatenated with 3 dense layers followed by a final softmax layer, employing a categorical cross-entropy loss function (Supplementary Fig 3, available via Mendeley at <https://data.mendeley.com/datasets/fh7sk5ksmk/2>). The feature extractors pretrained on ImageNet were obtained from Tensorflow Hub for weight initialization before full fine-tuning. Image augmentation, early stopping, and limiting to 200 epochs were used during training to prevent overfitting; separate models were trained at 40× and 100×.

**Primary and exploratory analyses.** Model set 1 - In this primary analysis, fully supervised learning models were trained on the images with tumor locations manually segmented by an experienced Mohs surgeon (E.T.). All models were trained on split tiles of 224 × 224 pixels. Each square tile was labeled as “positive” if the tumors occupied ≥10% of the area or categorized as controls. Extra controls were included from images of other diagnoses (eg, SCC to train BCC models and vice versa, actinic keratoses and normal skin).

To ensure that ground truth was reproducible, the concordance was estimated by comparing the segmentation masks prepared by 2 experienced Mohs surgeons (E.T.; D. Lim) and an anatomical pathologist (D. Lamont) on randomly selected 25 images. Interrater agreement was measured by Fleiss' kappa for identifying ≥5% tumor presence in each 50 × 50 pixel tile generated from the masks.

Model set 2 - Considering the labor-intensive manual segmentation process, we further evaluated in an exploratory analysis on whether models trained through weakly supervised learning (WSL) can achieve similar performance in region of interest detection in the subset of BCC 10× images; WSL has been known to achieve clinical-grade precision without requiring human annotations.<sup>24</sup> In this 2-stage approach, classifiers were first trained using all tiles labeled with the top-level diagnosis without expert annotations. The second

stage of the training selectively included only the tiles with high inferred probabilities from the first-step. The control image tiles remained unchanged during this process.

**Performance metrics and validation**

**studies.** The primary performance metric was the pixel-level area under the precision-recall curve (AUPRC), estimating the average precision across all prediction thresholds for each tumor type at the 40× and 100× magnifications. Secondary metrics include the area under the receiver-operating characteristic curve (AUROC), the highest Dice coefficient, and folds enrichment of precision (AUPRC divided by the proportion of positive pixels). To accurately assess these metrics on the probability maps, the ground truth masks were reshaped to fill the same boundaries prescribed by the deep learning algorithm. Additional explanation is provided in Supplementary Fig 4, available via Mendeley at <https://data.mendeley.com/datasets/fh7sk5ksmk/2>.

The internal model validity was assessed on model set 1 using leave-one-out cross-validation (LOOCV) on the subset of images where the ground truth has been annotated. To avoid contamination of information from images obtained from the same patient, each test fold was limited to a single patient (patient-level LOOCV). The external validity was estimated on the temporal validation cohort and stratified by magnification levels and model architectures. The CIs were estimated using ordinary bootstrap resampling over 10,000 iterations. The paired Wilcoxon test was used to compare the metrics between models on the same images; the type I error rate was set at 0.01 adjusted for multiple testing.

**Software.** All models were built on the TensorFlow framework 2.7.0. The preprocessing and evaluation tools were implemented using customized computer scripts. Descriptive statistics and the bootstrapping procedures were performed using the R Statistical Environment 4.0.

**RESULTS****Cohort and tumor characteristics**

Two hundred fifty-eight patients over 293 visits were screened. Digital FMV images for 220 patients were available and 1836 images were retrieved. The median age of the patient population was 61 years old (interquartile range, 58-76). One hundred eighty-seven patients (85%) were diagnosed with BCC, with nodular ( $n = 88$ ), infiltrative ( $n = 49$ ), and superficial ( $n = 20$ ) being the commonest subtypes. Thirty-three patients (15%) with SCC were identified including 1 patient with perineural invasion (Table I). Three patients (1%) had metachronous BCC and SCC.

**Table I.** Characteristics of the development and validation cohorts ( $N = 220$ )

| Clinical values                           | Development cohort<br>( $n = 154$ ) | Validation cohort<br>( $n = 66$ ) |
|---|-------------------------------------|-----------------------------------|
| Age group, y (%)                          |                                     |                                   |
| <40                                       | 7 (5)                               | 4 (6)                             |
| 41-60                                     | 44 (29)                             | 18 (27)                           |
| 61-80                                     | 78 (51)                             | 38 (57)                           |
| > 81                                      | 25 (16)                             | 6 (9)                             |
| Gender                                    |                                     |                                   |
| Male                                      | 84 (55)                             | 43 (65)                           |
| Female                                    | 70 (45)                             | 23 (35)                           |
| Tumor type                                |                                     |                                   |
| Basal cell carcinoma (BCC)                |                                     |                                   |
| Nodular BCC                               | 58 (38)                             | 30 (45)                           |
| Infiltrative BCC                          | 32 (21)                             | 17 (26)                           |
| Superficial BCC                           | 17 (11)                             | 3 (5)                             |
| Micronodular BCC                          | 12 (8)                              | 4 (6)                             |
| Morpheaform BCC                           | 5 (3)                               | 0 (0)                             |
| Basosquamous BCC                          | 2 (1)                               | 2 (3)                             |
| Nodulocystic BCC                          | 2 (1)                               | 1 (2)                             |
| Desmoplastic BCC                          | 0 (0)                               | 1 (2)                             |
| Squamous cell carcinoma (SCC)             | 26 (17)                             | 8 (12)                            |
| Location of the tumor                     |                                     |                                   |
| Nose                                      | 61 (40)                             | 32 (48)                           |
| Ear                                       | 19 (12)                             | 9 (14)                            |
| Cheek, forehead, and temple               | 44 (28)                             | 11 (18)                           |
| Lip                                       | 11 (7)                              | 2 (3)                             |
| Periocular, eyelid, and eyebrow           | 12 (8)                              | 9 (15)                            |
| Scalp (frontal, vertex, or occipital)     | 5 (3)                               | 0 (0)                             |
| Other                                     | 2 (1)                               | 3 (6)                             |
| No. of Mohs procedures                    |                                     |                                   |
| 1   | 133 (86)                            | 60 (91)                           |
| 2   | 16 (10)                             | 6 (9)                             |
| $\geq 3$                                  | 5 (3)                               | 0 (0)                             |
| No. of images per patient, median (range) | 7 (0-35)                            | 6 (0-52)                          |
| No. (%) with annotated images             | 79 (51)                             | 66 (100)                          |
| No. (%) of Mohs stages                    |                                     |                                   |
| 1   | 44 (29)                             | 43 (65)                           |
| 2   | 85 (55)                             | 18 (27)                           |
| 3   | 16 (10)                             | 2 (3)                             |
| $\geq 4$                                  | 9 (6)                               | 3 (5)                             |

Most tumors were located on the nasal region ( $n = 93$ , 42%), with nasal ala and tips being the most frequent sites involved ( $n = 59$ , 27%) followed by the dorsum and sidewall ( $n = 27$ , 12%). A median of 1 surgical procedure per patient was performed (range 1-5), with the median number of MMS stages of 2 (range 1-8). The median size of lesions before MMS was 1.4 cm (range 0.2-4.5). The full cohort and tumor characteristics are shown in Table I.

Based on the date of the project initiation, 154 patients (70%) were assigned into the development cohort and 66 patients (30%) assigned to the temporal validation cohort (Fig 1). The validation cohort was similar to the training cohorts with respect to demographic, pathology, and tumor subtypes, except for the lower number of MMS stages per operation ( $P < .001$ ,  $\chi^2$  test).

### Concordance of tumor localization in frozen section images

Estimated using 25 FMV images (23 BCC and 2 SCC), the interannotator agreement between segmentation masks was high (mean Fleiss' Kappa 0.877, 95% CI 0.842-0.911). Each segmentation task required 20 to 30 minutes to complete. Further discussion on the concordance among specialists is presented in Supplementary Fig 5, available via Mendeley at <https://data.mendeley.com/datasets/fh7sk5ksmk/2>.

### Model development and cross-validation analysis

**BCC**—a total of 267 images at 100 $\times$  magnification level in 66 (of 154) patients had been annotated, with 241 images (90%) in 59 patients containing  $\geq 10\%$  of the nontumor region that is considered suitable for LOOCV (59-fold) analysis. The median AUPRC were 0.939 (95% CI: 0.923-0.953) for EfficientNet and 0.949 (0.932-0.960) for MobileNet, equivalent to a median of 2.56 (2.45-2.71) and 2.67-fold (2.52-2.84) more likely to correctly locate the lesions than at random. Both architectures showed strong discrimination, as evidenced by high median AUROCs of 0.900 (0.873-0.923) and 0.917 (0.904-0.931, Supplementary Table VI, available via Mendeley at <https://data.mendeley.com/datasets/fh7sk5ksmk/2>); the corresponding median Dice coefficients were 0.892 (0.883-0.903) and 0.897 (0.888-0.907).

Highly concordant performances were seen at the 40 $\times$  magnification level. In 147 of 149 images (99%) suitable for the LOOCV analysis, we observed high median AUPRCs of 0.944 for both EfficientNet and MobileNet, equivalent to a median of 4-fold enrichment of precision over the baseline. The median AUROC were 0.954 (0.942-0.970) and 0.948 (0.926-0.968), with median Dice coefficients of 0.899 (0.884-0.911) and 0.897 (0.870-0.909), for both architectures respectively (Supplementary Table VI, available via Mendeley at <https://data.mendeley.com/datasets/fh7sk5ksmk/2>).

**SCC**—in 23 patients with SCC, the segmented masks for 13 cases (31 images for 100x and 12 for 40x) were available for LOOCV. For 25 images (80%)

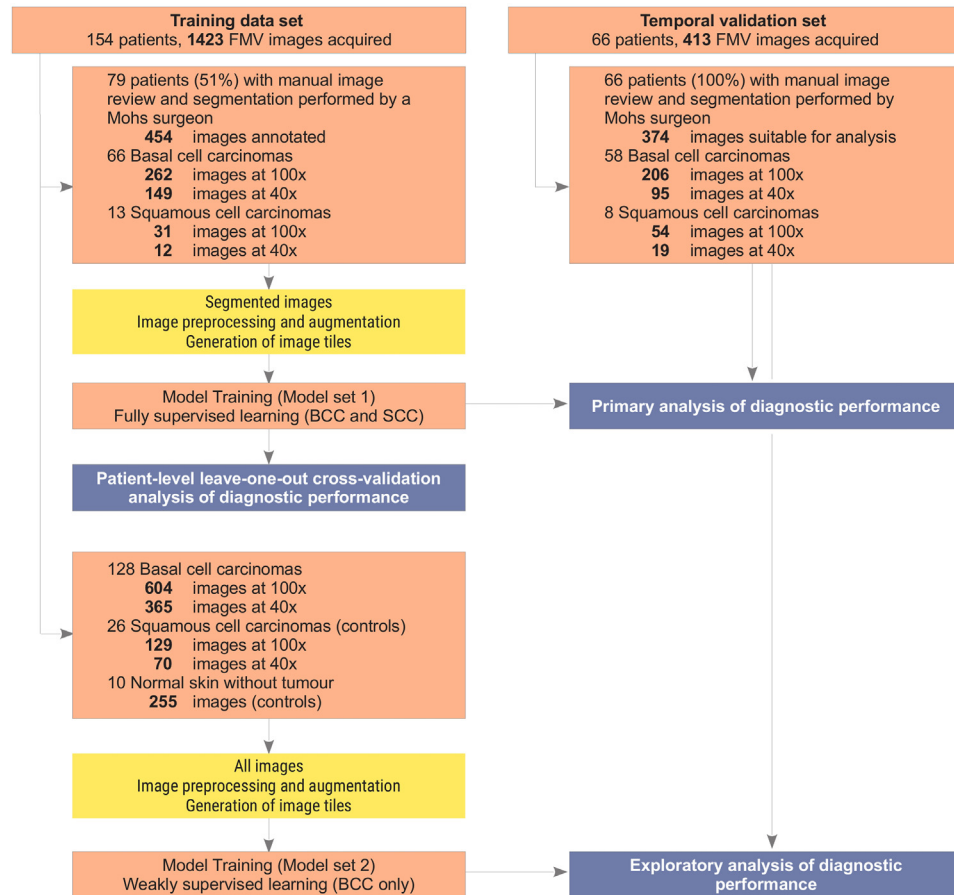


**Fig 1.** Flowchart of data analysis. *BCC*, Basal cell carcinoma; *FMV*, focused microscope view; *SCC*, squamous cell carcinoma.

containing  $\geq 10\%$  of the nontumor region, the AUPRC for the 100x models were 0.910 (0.878-0.963) for EfficientNet and 0.920 (0.888-0.980) for MobileNet. The median folds enrichment of precision were 2.66 (2.41-3.12) and 2.74 (2.28-3.30) respectively. The median AUROCs were 0.903 (0.795-0.939) and 0.912 (0.834-0.960), and the Dice coefficients were 0.929 (0.887-0.973) and 0.959 (0.878-0.973), for the 2 models (Supplementary Table VI, available via Mendeley at <https://data.mendeley.com/datasets/fh7sk5ksmk/2>).

Only 7 of 12 images were suitable for LOOCV at 40x. Moderate AUPRCs were achieved (median 0.795 for EfficientNet, 0.560-0.927, and 0.701 for MobileNet, 0.336-0.979). The respective AUROCs were 0.747 (0.678-0.877) and 0.768 (0.448-0.981).

### Performance of region of interest detection by model set 1 in temporal validation cohort

The validation cohort included 66 patients with NMSC with expert-annotated FMV images. In 58 patients with BCC (206 images for 100x

magnification level; 95 for 40x), the saliency maps located BCC with high median AUPRC (0.966 for 100x, 0.957-0.972; 0.943 for 40x, 0.919-0.958) and AUROC (0.889 for 100x, 0.869-0.904 and 0.922 for 40x, 0.905-0.948). Per-image analysis revealed no performance difference between the EfficientNet and MobileNet at 100x (median difference in AUPRC 0.00013,  $P = .23$ ; in AUROC 0.0021,  $P = .11$ , paired Wilcoxon's test), although higher precision and discrimination were seen in EfficientNet models at 40x (median difference in AUPRC 0.0069,  $P = .009$ ; in AUROC: 0.016,  $P = .0034$ , Table II and Fig 2). Examples of the saliency maps are shown in Fig 3.

High precision was also evident in the SCC model at 100x magnification (median AUPRC 0.904, 0.851-0.936) with moderate discriminability (median AUROC 0.767, 0.700-0.865). No differences were observed in AUPRC between MobileNet and EfficientNet (median difference in AUPRC  $-0.009$ ,  $P = .10$ , and in AUROC  $-0.031$ ,  $P = .03$ ). Only modest AUPRC (median 0.536, 0.38-0.81) and AUROC

**Table II.** Performance of the best performing deep learning models for detecting regions-of-interest in the temporal validation cohort

| Model and testing images                | AUPRC               | AUROC               | Dice coefficient    | FEP              |
|---|---------------------|---------------------|---------------------|------------------|
| Basal cell carcinoma (BCC, $n = 58$ )   |                     |                     |                     |                  |
| 100× images (206)                       |                     |                     |                     |                  |
| 100× model, median (CI)                 | 0.966 (0.957-0.972) | 0.889 (0.869-0.904) | 0.942 (0.937-0.945) | 2.31 (2.23-2.42) |
| 40× images (95)                         |                     |                     |                     |                  |
| 40× model, median (CI)                  | 0.943 (0.919-0.958) | 0.922 (0.905-0.948) | 0.900 (0.875-0.918) | 3.27 (2.7-4.06)  |
| 100× model, median (CI)                 | 0.843 (0.801-0.897) | 0.897 (0.871-0.915) | 0.794 (0.763-0.839) | 3.35 (2.84-4.33) |
| Squamous cell carcinoma (SCC, $n = 8$ ) |                     |                     |                     |                  |
| 100× images (54)                        |                     |                     |                     |                  |
| 100× model, median (CI)                 | 0.904 (0.851-0.936) | 0.767 (0.700-0.865) | 0.915 (0.849-0.93)  | 2.19 (2.12-2.49) |
| 40× images (19)                         |                     |                     |                     |                  |
| 40× model, median (CI)                  | 0.635 (0.38-0.814)  | 0.577 (0.520-0.706) | 0.680 (0.532-0.918) | 1.86 (1.3-2.02)  |

AUPRC, Area under the precision-recall curve; AUROC, area under the receiver operating characteristic curve; FEP, folds enrichment of precision.

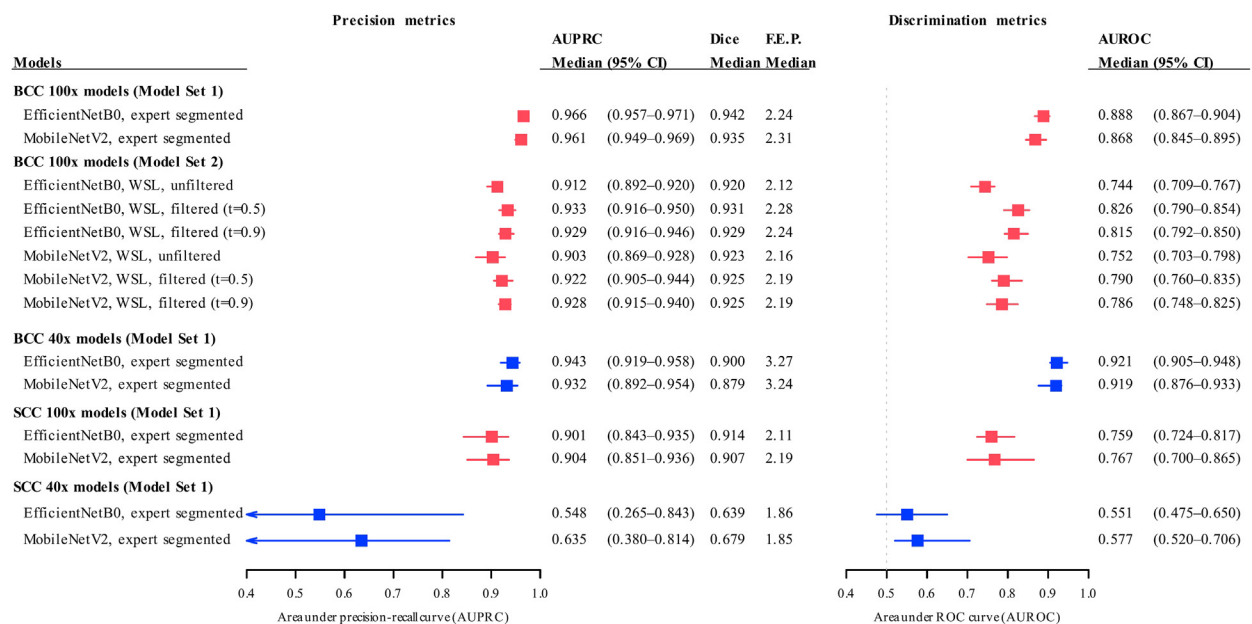


**Fig 2.** Performance of deep learning models stratified by model sets, architecture, training data, and training method. AUPRC, Area under the precision-recall curve; AUROC, area under the receiver operating characteristic curve; BCC, basal cell carcinoma; Dice, Dice coefficient; FEP, folds enrichment of precision; SCC, squamous cell carcinoma; WSL, weakly supervised learning.

(median 0.577, 0.520-0.706) was achieved by the best 40× models.

Resizing 40× BCC images to 100× resulted in similar level of discriminability (median AUROC: 0.897, 0.869-0.904, median pairwise difference  $-0.014$  vs the 40× model,  $P = .21$ ) but lowered precision (median AUPRC 0.843, 0.801-0.897, median difference  $-0.039$ ,  $P < .001$ ). The model performance was uniform across the BCC subtypes with  $>10$  samples (Supplementary Table VII,

available via Mendeley at <https://data.mendeley.com/datasets/fh7sk5ksmk/2>).

### Exploratory analysis on the temporal validation set for model set 2

The WSL models showed high precision in region of interest detection with an AUPRC  $>0.9$ , albeit with lower AUPRC and AUROC compared to models in model set 1 (Fig 3). For example, WSL models at the filtering threshold  $t = 0.5$  showed lower

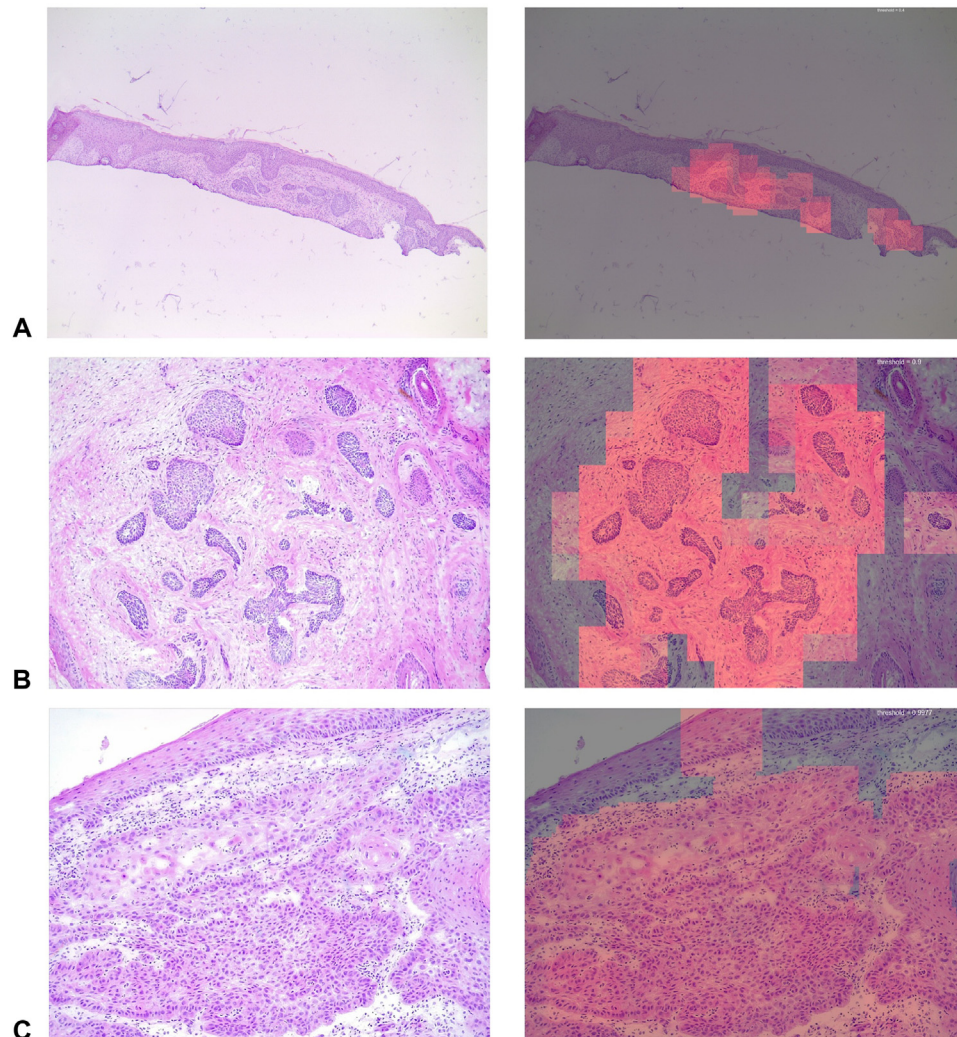


**Fig 3.** Example of probability map produced by the deep learning models for detection of nonmelanoma skin cancer in Mohs frozen sections. **A**, Nodular BCC, 40×, with saliency maps produced by EfficientNet B0 100× model (pixel level AUPRC: 0.826, AUROC 0.981). **B**, Micronodular BCC, 100×, MobileNet V2 100× model (AUPRC 0.996, AUROC 0.991). **C**, Squamous cell carcinoma, 100× model, MobileNet V2 (AUPRC 0.991, AUROC 0.912). All deep learning models were trained with full supervised learning (model set 1).

discriminability in both EfficientNet (AUROC 0.826, median pairwise difference  $-0.042$ ,  $P < .001$ ) and MobileNet (AUROC 0.790, median difference  $-0.046$ ,  $P < .001$ ) architectures.

## DISCUSSION

The central finding of this study is that deep learning locates NMSCs on digitized images of Mohs frozen sections with high accuracy and efficiency supporting the use of AI-assisted margin control as a “second read” to reduce human error.<sup>5</sup>

A recent study has shown a comparable performance from the whole slide images of BCC acquired using a digital slide scanner.<sup>18</sup> Despite the commercial availability, the cost of scanners remains prohibitive to

many clinics and not justifiable for low-volume centers. A software-assisted review of FMV images could be implemented in any Mohs laboratory at a fraction of the latter cost, reusing only inexpensive microscope systems. Such an AI approach would be expected to have maximum utility when integrated with a built-in slide scanner, in-effect eliminating the need to examine frozen section slides altogether though further evidence will be needed to corroborate the value and safety of this approach. Recent proof-of-concept studies support the findings of this study but are limited by the lack of evaluation of performance metrics in clinical cohorts.<sup>24-26</sup>

The present study provides several valuable insights into AI data quality. First, reviewing

discrepancies among specialists is necessary to understand how the causes of over- or under-diagnosis occur during single-pass pathology review. For example, distinguishing between a hair follicle and tumor in BCC, or between inflammatory cells and tumor in SCC, can be challenging. In the real-world setting, the Mohs surgeon and pathologist may review multiple wafers or different pathologic levels. Transparent annotations are imperative in understanding the constraints of applicability of AI-based models, given that variations in diagnostic labels are likely to hinder the reproducibility of results.<sup>27</sup>

Second, although validations at external sites are planned, the work presented here supports the feasibility of site-specific diagnostic models based on reutilization of archival images from medical records. Third, our research highlights the importance of involving surgeons and pathologists in the creation of accurate ground truth annotations to achieve good classification results. This manual semantic segmentation is a tedious task that often acts as the rate-limiting step in model development due to its high-level of precision and the need for expert knowledge in making a diagnosis. Further investigations into alternative methods for automation, such as WSL, may overcome this limitation.

Our study has several limitations. Microscopic images were taken in a single Mohs unit; variations in surgical techniques, sample preparation, and imaging acquisition methods could thus impact model accuracy at other sites. Furthermore, only microscopic views at the standard resolution used by Mohs surgeons were analyzed; visualizing the complete section at high resolutions through whole slide analysis could improve margin control. Moreover, in contrast to the good performance of the BCC models, insufficient data hampered SCC model performance at 40x magnification in our study, highlighting the importance of adequate training data. Image sharing across Mohs units may facilitate collaborative model development for tumor types less frequently seen.

Immunohistochemical staining was not performed in this Mohs unit. Future studies should include this assessment, particularly given that there is increasing interest in managing melanoma with MMS. Lastly, our tile-based classification paired with custom evaluation metrics was designed to maximally leverage the 3-dimensional spatial context of tumors to identify hidden or unseen tumor areas. This spatial understanding is vital for Mohs surgery as unexpected inflammation or fibrosis may be a harbinger of tumor necessitating another stage.<sup>28,29</sup> Future studies will benchmark our models against

segmentation approaches like U-net,<sup>30</sup> to also assess its effectiveness in prospective trials in overall margin control beyond accurate localization.

In conclusion, this study supports the accuracy of deep learning models for detecting NMSCs on Mohs frozen sections. Prospective studies in accordance with CONSORT-AI and SPIRIT-AI guidelines will determine the acceptable bar for adoption as a diagnostic support tool during real-time tumor removal.

## DATA AVAILABILITY STATEMENT

The software code is made publicly available on GitHub repository (<https://github.com/fpylin/MohsAI>). The dataset can be obtained from the authors upon request, subject to additional reviews by relevant Human Research Ethics Committees and Institutional Review Boards.

The authors thank El Reilly for graphical assistance in preparation of the graphical abstract.

## Conflicts of interest

None disclosed.

## REFERENCES

1. NCCN. Clinical. Practice Guidelines Basal Cell Skin Cancer. National Comprehensive Cancer Network; 2022.
2. NCCN. Clinical. Practice Guidelines Squamous Cell Skin Cancer. National Comprehensive Cancer Network; 2022.
3. Tan E, Elliott T, Yu L, Litterick K. Mohs surgery histopathology concordance in Australia. *Australas J Dermatol*. 2011;52:245-247. <https://doi.org/10.1111/j.1440-0960.2011.00755.x>
4. Mariwalla K, Aasi SZ, Glusac EJ, Leffell DJ. Mohs micrographic surgery histopathology concordance. *J Am Acad Dermatol*. 2009;60:94-98. <https://doi.org/10.1016/j.jaad.2008.09.061>
5. Wee E, Goh MS, Estall V, et al. Retrospective audit of patients referred for further treatment following Mohs surgery for non-melanoma skin cancer. *Australas J Dermatol*. 2018;59:302-308. <https://doi.org/10.1111/ajd.12779>
6. Wallace JS, Bond JS, Seidel GD, Samie FH. An important mimicker: plaque-type syringoma mistakenly diagnosed as microcystic adnexal carcinoma. *Dermatol Surg*. 2014;40(7):810-812. <https://doi.org/10.1111/DSU.0000000000000042>
7. Rutherford T, Elliott T, Vinciullo C. Mohs surgery in Australia: a survey of work practices. *Australas J Dermatol*. 2011;52:98-103. <https://doi.org/10.1111/j.1440-0960.2011.00751.x>
8. Coudray N, Ocampo PS, Sakellaropoulos T, et al. Classification and mutation prediction from non-small cell lung cancer histopathology images using deep learning. *Nature medicine*. 2018;24:1559-1567. <https://doi.org/10.1038/s41591-018-0177-5>
9. Komorowski M, Celi LA, Badawi O, Gordon AC, Faisal AA. The artificial intelligence clinician learns optimal treatment strategies for sepsis in intensive care. *Nature medicine*. 2018;24:1716-1720. <https://doi.org/10.1038/s41591-018-0213-5>
10. Niazi MKK, Parwani AV, Gurcan MN. Digital pathology and artificial intelligence. *Lancet Oncol*. 2019;20:e253-e261. [https://doi.org/10.1016/S1470-2045\(19\)30154-8](https://doi.org/10.1016/S1470-2045(19)30154-8)
11. Dreiseitl S, Binder M, Hable K, Kittler H. Computer versus human diagnosis of melanoma: evaluation of the feasibility of an automated diagnostic system in a prospective clinical trial.

- Melanoma Res.* 2009;19:180-184. <https://doi.org/10.1097/CMR.0b013e32832a1e41>
12. Esteva A, Kuprel B, Novoa RA, et al. Dermatologist-level classification of skin cancer with deep neural networks. *Nature.* 2017;542:115-118. <https://doi.org/10.1038/nature21056>
  13. Ferrante di Ruffano L, Takwoingi Y, Dinnes J, et al. Computer-assisted diagnosis techniques (dermoscopy and spectroscopy-based) for diagnosing skin cancer in adults. *Cochrane Database Syst Rev.* 2018;12:CD013186. <https://doi.org/10.1002/14651858.CD013186>
  14. Haenssle HA, Fink C, Schneiderbauer R, et al. Man against machine: diagnostic performance of a deep learning convolutional neural network for dermoscopic melanoma recognition in comparison to 58 dermatologists. *Ann Oncol.* 2018;29:1836-1842. <https://doi.org/10.1093/annonc/mdy166>
  15. Premaladha J, Ravichandran KS. Novel approaches for diagnosing melanoma skin lesions through supervised and deep learning algorithms. *J Med Syst.* 2016;40:96. <https://doi.org/10.1007/s10916-016-0460-2>
  16. Tschandl P, Rosendahl C, Akay BN, et al. Expert-level diagnosis of nonpigmented skin cancer by combined convolutional neural networks. *JAMA dermatology.* 2019;155:58-65. <https://doi.org/10.1001/jamadermatol.2018.4378>
  17. Hekler A, Utikal JS, Enk AH, et al. Deep learning outperformed 11 pathologists in the classification of histopathological melanoma images. *Eur J Cancer.* 2019;118:91-96. <https://doi.org/10.1016/j.ejca.2019.06.012>
  18. van Zon MCM, van der Waa JD, Veta M, Krekels GAM. Whole-slide margin control through deep learning in Mohs micrographic surgery for basal cell carcinoma. *Experimental dermatology.* 2021;30:733-738. <https://doi.org/10.1111/exd.14306>
  19. Daneshjou R, Barata C, Betz-Stablein B, et al. Checklist for evaluation of image-based artificial intelligence reports in dermatology: CLEAR derm consensus guidelines from the international skin imaging collaboration artificial intelligence working group. *JAMA dermatology.* 2022;158:90-96. <https://doi.org/10.1001/jamadermatol.2021.4915>
  20. Collins GS, Reitsma JB, Altman DG, Moons KG. Transparent reporting of a multivariable prediction model for individual prognosis or diagnosis (TRIPOD): the TRIPOD statement. *Ann Intern Med.* 2015;162:55-63. <https://doi.org/10.7326/M14-0697>
  21. Larson K, Ho HH, Anumolu PL, Chen TM. Hematoxylin and eosin tissue stain in Mohs micrographic surgery: a review. *Dermatol Surg.* 2011;37:1089-1099. <https://doi.org/10.1111/j.1524-4725.2011.02051.x>
  22. Tan M, Le QV. EfficientNetV2: smaller models and faster training. *International Conference on Machine Learning.* 2021. <https://doi.org/10.48550/arXiv.2104.00298>
  23. Sandler M, Zhu HM, Zhmoginov A, Chen LC. MobileNetV2: inverted residuals and linear bottlenecks. 2018 IEEE/CVF Conference on Computer Vision and Pattern Recognition. 2018:4510-4520. <https://doi.org/10.1109/CVPR.2018.00474>
  24. Campanella G, Nehal KS, Lee EH, et al. A deep learning algorithm with high sensitivity for the detection of basal cell carcinoma in Mohs micrographic surgery frozen sections. *J Am Acad Dermatol.* 2021;85:1285-1286. <https://doi.org/10.1016/j.jaad.2020.09.012>
  25. Bonnefille H, Abbas M, Roger P, et al. A deep-learning algorithm to localize basal cell carcinoma foci on Mohs surgery frozen sections. *J Eur Acad Dermatol Venereol.* 2023; 37:e631-e632. <https://doi.org/10.1111/jdv.18859>
  26. Sohn GK, Sohn JH, Yeh J, Chen Y, Brian Jiang SI. A deep learning algorithm to detect the presence of basal cell carcinoma on Mohs micrographic surgery frozen sections. *J Am Acad Dermatol.* 2021;84:1437-1438. <https://doi.org/10.1016/j.jaad.2020.06.080>
  27. Daneshjou R, Smith MP, Sun MD, Rotemberg V, Zou J. Lack of transparency and potential bias in artificial intelligence data sets and algorithms: a scoping review. *JAMA dermatology.* 2021;157:1362-1369. <https://doi.org/10.1001/jamadermatol.2021.3129>
  28. Alam M, Khan M, Veledar E, et al. Correlation of inflammation in frozen sections with site of nonmelanoma skin cancer. *JAMA dermatology.* 2016;152:173-176. <https://doi.org/10.1001/jamadermatol.2015.3649>
  29. Macdonald J, Sneath JR, Cowan B, Zloty D. Tumor detection after inflammation or fibrosis on Mohs levels. *Dermatol Surg.* 2013;39:64-66. <https://doi.org/10.1111/dsu.12012>
  30. Ronneberger O, Fischer P, Brox T. U-Net: Convolutional Networks for Biomedical Image Segmentation. Springer International Publishing; 2015:234-241.